1993ApJ...417..415C

THE ASTROPHYSICAL JOURNAL, 417:415–426, 1993 November 10
© 1993. The American Astronomical Society. All rights reserved. Printed in U.S.A.

COLD DARK MATTER COSMOGONY WITH HYDRODYNAMICS AND GALAXY FORMATION: GALAXY PROPERTIES AT REDSHIFT ZERO

RENYUE CEN AND JEREMIAH P. OSTRIKER
Princeton University Observatory, Princeton, NJ 08544
Received 1992 December 31; accepted 1993 May 17

ABSTRACT

We have supplemented our code, which computes the evolution of the physical state of a representative piece of the universe, to include not only the dynamics of dark matter (with a standard PM code) and the hydrodynamics of the gaseous component (including detailed collisional and radiative processes), but also galaxy formation on a heuristic but plausible basis. If, within a cell, the gas is Jeans-unstable, collapsing and cooling rapidly, it is transformed to galaxy subunits, which are then followed with a collisionless code. We study two representative boxes with sizes $L = (80, 8)\ h^{-1}$ Mpc, in both cases utilizing a mesh of 200^3 cells containing 200^3 dark matter particles and having nominal resolutions of $(400, 40)\ h^{-1}$ kpc, respectively, with true resolution approximately 2.5 times worse. We adopt the standard cold dark matter (CDM) perturbation spectrum with an amplitude of $\sigma_8 \equiv (\delta M/M)_{\rm rms,8} = 0.77$, a compromise between the *COBE* normalization $\sigma_8 = 1.05$ and that indicated by the small-scale velocity dispersion (perhaps $\sigma_8 = 0.45$).

We find a mass function which is similar to that observed. There is a strong correlation between galactic age and environment. Identifying the oldest fraction with elliptical and S0 galaxies, we find a density morphology relation of the same type as is observed as well as a correlation between gas mass/total mass ratio and morphology that is similar to observations. In addition, we find that low-mass galaxies contain relatively more dark matter than giants.

We present analytic fits to our derived results for "bias," the dependence of $\rho_{\rm gal}/\langle\rho_{\rm gal}\rangle$ on $\rho_{\rm tot}/\langle\rho_{\rm tot}\rangle$. Spatial structures resemble quantitatively those seen in redshift surveys, with galaxies concentrated in clusters and on filaments (or sheets) which surround quite empty voids. The void probability statistics indicate that this model is consistent with magnitude-limited real data.

The small-scale velocity field is too large compared with the observed velocity correlation function. The distribution of proper velocities fits an exponential (not a Maxwellian) $P(v) \propto v^2 e^{-v/\sigma_{\rm exp}}$ with $\sigma_{\rm exp} = 225$ km s^{-1}. For galaxies separated by $1\ h^{-1}$ Mpc we find a one-dimensional velocity dispersion of 670 km s^{-1} (490 km s^{-1} for the most massive subset) compared with 340 ± 40 km s^{-1} as measured by Davis & Peebles (1983). Adoption of the *COBE* normalization causes the problem to become worse; the CDM prediction is then approximately (920 ± 160) km s^{-1}.

If we look at the genus curves of all our galaxies, they fit the random-phase expectation, but a magnitude-limited sample emphasizes the older, more massive galaxies which have collected at a vertices. This explains the observed "meatball shift" of the genus curves found in observed samples.

Subject headings: cosmology: theory — dark matter — galaxies: formation — hydrodynamics — large-scale structure of universe

1. INTRODUCTION

Most theoretical treatments of large-scale structure have been based on N-body simulations of the interactions among collisionless "dark matter" particles. This was done for two reasons: first, because, in the theories considered, the principal component was in fact some dark, collisionless set of noninteracting particles which were properly treated in this fashion and, second, because hydrodynamics, which is needed for the gaseous component, is difficult and messy. We have developed over a period of years a hydrodynamic code which, while still seriously lacking in sufficient numerical resolution, has gradually incorporated within it much of the relevant physics. Gravity is treated in the particle-mesh plus cloud-in-cell manner, which, while not having the resolution of the P^{3}M formalism, is very fast and efficient, allowing very large simulations to be run. The hydro code is based on a well-tested aerodynamic code of Jameson (1989), which has been extensively modified and tested for use in cosmological applications (cf. Cen 1992). Radiation and collisional processses among all species of a hydrogen and helium plasma of primordial composition are followed in full (nonequilibrium) detail, with the radiation field also treated in detail (with regard to frequency), but on a spatially averaged basis.

In a series of papers we have utilized this code to explore the various popular cosmogonic scenarios at the common standard of $128^3 = 10^{6.3}$ particles and cells with the standard CDM scenario treated in Cen & Ostriker (1992a, hereafter CO92). To proceed further, it is necessary to allow for galaxy formation in some fashion. Some prior work has been done in this area by Baron & White (1987), Suto, Itoh, & Inagaki (1990), and others using the Press-Schechter formalism. In the paper preceding this one (Cen & Ostriker 1993, hereafter Paper II), we increased our resolution to $200^3 = 10^{6.9}$ particles and cells and adopted the straightforward "brute force" approach of incorporating galaxy formation into our hydro code.

In brief (details given in Cen & Ostriker 1992b, hereafter Paper I), when, in a cell, matter is cooling and gravitationally

© American Astronomical Society • Provided by the NASA Astrophysics Data System

1993ApJ...417..415C

collapsing toward its center on a timescale $t_{\rm dyn} = (3\pi/32G\rho_{\rm tot})^{1/2}$, where $\rho_{\rm tot}$ is the total matter density in the cell, then, in the next time step Δt, we remove baryons from that cell in amount $m_* = m_b \Delta t/t_{\rm dyn}$ and create a collisionless particle within the cell of that mass and with the mean velocity of the gas of the cell. Each particle at birth is labeled with its mass m_*, the cosmic time at its birth t_i, and the dynamical time in its birth cell $t_{\rm dyn}$. These galaxy subunits are then followed with the same collisionless code, which follows the dark matter, so that they feel the gravity due to local and large-scale gas, dark matter and other galaxies. We can at any point group the subunits with an adaptive friends-of-friends clustering algorithm to construct catalogs of galaxies and clusters. For each galaxy we can find the mass-weighted average for birth epoch $\langle t_i \rangle$ and other properties derived from the labeled subunits.

Thus we can follow galaxy formation as a function of time and space, not relying on dark matter halos to be proxies for galaxies. After the fact we can, of course, check how well the galaxy and dark matter properties correlate (cf. § 3). In a first discussion of this work we concentrated on the temporal aspects of galaxy formation and on the issue of physical bias (Paper I). In Paper II we discussed the aspects of the problem related to the integalactic medium (IGM). Here we focus on the structures seen in the galaxy distribution at low redshift.

We are treating the popular standard cold dark matter model first in this paper, not because we believe it to be correct but because it is popular and because it does a creditable if not perfect job of matching many of the observations. We choose an amplitude for the spectrum that is most favorable to the theory, not so low that it is grossly inconsistent with the *COBE* normalization and not so high that it too grossly violates small-scale velocity limits.

The organization of this paper is conventional, with § 2 detailing the methods, § 3 giving results, and § 4 presenting our conclusions.

2. METHOD AND INITIAL CONDITIONS

The numerical methods and treatment of detailed atomic physics are described in Cen (1992) and in CO92. To summarize briefly, we use a hydro code based on Jameson's (1989) aerospace code, modified extensively for cosmological applications. Poisson's equation is solved on a periodic mesh using an efficient fast Fourier transform (FFT) routine. All the principal line and continuum atomic processes are computed for each cell and each time step for a plasma of standard composition. The radiation field from 1 eV to 100 keV is treated in detail with allowance for sources, sinks, and cosmological effects, but only in a spatially averaged fashion. What is new here is that we attempt to model galaxy formation in a heuristic but plausible way. The details of how we identify galaxy formation, follow the motion of formed galaxies, and treat feedback processes (UV and supernova energy input into the IGM from young massive stars) were presented in an earlier paper (cf. § 2 in Paper I).

We adopt standard CDM parameters $h = 0.5$, $\Omega = 1$, $\Omega_b = 0.06$, and $\sigma_8 = 0.77$. The amplitude chosen is a compromise: while it is somewhat (35%, or approximately 2 σ) below the *COBE* normalization (Efstathiou, Bond, & White 1992), it is approximately 2 σ above the value indicated by the small-scale velocity field. Our box size is 80 h^{-1} Mpc, so with 200^3 cells and dark matter particles our nominal resolution is 400 h^{-1} kpc, but the actual resolution, as determined by extensive tests (Cen 1992), is approximately a factor of 2.5 worse than this (~ 1 h^{-1} Mpc). The adopted value of Ω_b follows from standard light-element nucleosynthesis (Walker et al. 1991) and our chosen value of h.

How do we construct the galaxies out of the collisionless subunits formed in cooling collapsing regions? Because of our relatively poor spatial resolution (0.4 h^{-1} Mpc), the scale of a galaxy is not as distinct from the intergalaxy separation scale as it is in the real world. The standard, friends-of-friends linking scheme uses a global linking length, which has the defect that it overlinks dense regions and underlinks underdense regions. In order to avoid this problem, we use an adaptive friends-of-friends linking scheme to join together neighboring particles into galactic units. We determine the linking length b_{ij} between ith and jth particles by

$$b_{ij} = \text{Min}\left\{\frac{L_{\rm box}}{N^{1/3}},\ \beta L\left(\frac{\bar{\rho}}{2}\right)^{1/3}\left[\frac{1}{\rho_i(a_s)} + \frac{1}{\rho_j(a_s)}\right]^{1/3}\right\}, \quad (1)$$

where $L_{\rm box}$ is the box size, $\bar{\rho}$ is the mean mass density, and $\rho_i(a_s)$ denotes a local mass density at the ith particle position smoothed over a Gaussian window of radius a_s. There are two parameters we must use to obtain a linked list of galaxies: a_s and β, where a_s is the radius of the Gaussian smoothing window which is used to smooth the galaxy masses to obtain densities. Experiments with various values of these two parameters indicate that the final galaxies do not sensitively depend on the value of a_s, and we found that $a_s = 5$ h^{-1} Mpc is adequate for this purpose. However, the resulting galaxies from the linking scheme do depend on β. Figure 1*a* shows the final galaxy mass functions for the larger box and three values of β: 0.05, 0.10, 0.15. Also shown (*open squares*) is the mass function for the smaller box and $\beta = 0.10$. We find that $\beta = 0.10$ is the optimal value. Figure 1*b* shows the combined (small box plus large box) mass function compared with the Schechter function having $M_B/L = 3$. The fit is adequate in the sense that the number density of L^* or brighter galaxies in the simulation is roughly consistent with the observed value but not especially good, and we are at a loss to say whether this is due to our poor resolution or to a failure of the CDM scenario. In any case, our adopted values of (a_s, β) give us a volume density of galaxies comparable to that observed.

3. RESULTS

3.1. *Galaxy Properties*

Having defined the galaxies, let us examine their properties. Figure 1 shows a comparison between the mass function and the observed mass functions for various linking parameters. There are too many massive galaxies (our Local Group would be one galaxy), but for most purposes, where we will smooth on at least a 1 h^{-1} Mpc scale, this is a relatively unimportant defect and the derived mass function is adequate. Each galaxy is also labeled with $\langle t_i \rangle$, the mass-weighted average era of formation of its galactic subunits. In Figure 2*a* we show the histogram of birth epochs, and in Figure 2*b* the relation between mass and age. Finally, in Figure 2*c* we look at the ratio of the mass in cool gas ($T < 5 \times 10^5$ K) to the galaxy mass as a function of the era of galaxy formation. Examination of Figure 2 shows several interesting trends. Although much galaxy formation is very recent, with a peak at $z = 3$–2 and a peak in the star formation value (cf. PB) at $z = 2$–1, there is a nontrivial amount of galaxy formation at quite early epochs $z = 8$–5. The galaxies which are formed earlier tend to be significantly more massive than those formed later (Fig. 2*b*),

© American Astronomical Society • Provided by the NASA Astrophysics Data System

1993ApJ...417..415C

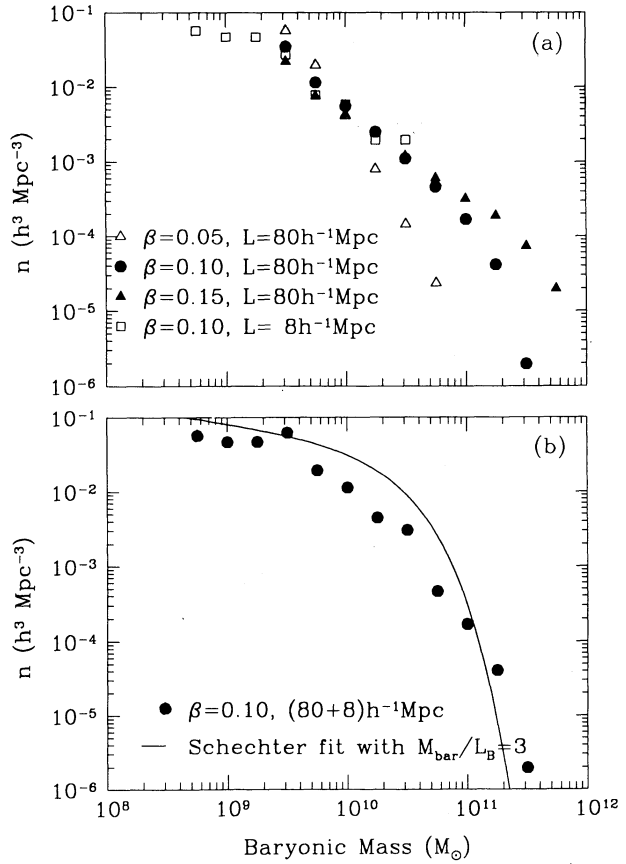

FIG. 1.—(*a*) Final galaxy mass functions for the 80 h^{-1} Mpc box with three values of β (the linking parameter): 0.05 (*open triangles*), 0.10 (*filled circles*), and 0.15 (*filled triangles*); also shown for $\beta = 0.10$ and the small box (*open squares*). Adopting $\beta = 0.10$ and combining the results from the two boxes, we obtain the filled circles in (*b*), where we also show a Schechter function with $M_{bar}/L_B = 3$. The fit is adequate in the sense that the number density of galaxies with L^* or brighter galaxies in the simulation is roughly consistent with the observed value.

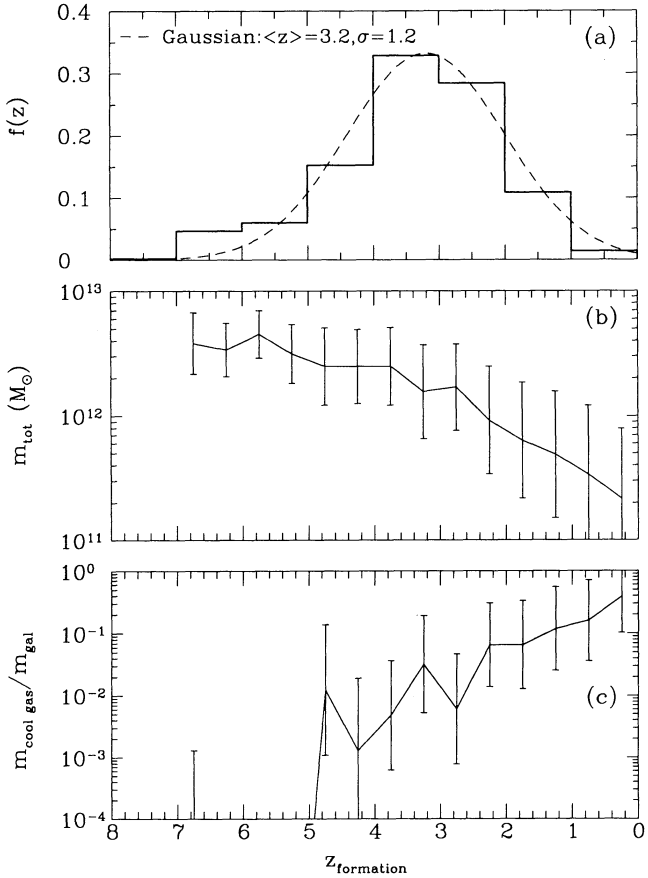

FIG. 2.—(*a*) Histogram of birth epochs. Also shown is a Gaussian fit to the histogram (*dashed line*). (*b*) Relation between galactic mass and the galaxy formation epoch: massive galaxies are formed earlier and dwarfs later. Error bars are 1 σ indicators. (*c*) Ratio of the mass in cool gas ($T < 5 \times 10^5$ K) to the galaxy mass as a function of the era of galaxy formation: gas-rich galaxies are young.

owing both to their initial masses and to subsequent mergers, and the amount of cool ($T < 5 \times 10^5$ K) gas associated with galaxies is much greater for recently formed systems than for old ones (Fig. 2*c*). There is, of course, a broad logarithmic scatter about these trends as indicated by the 1 σ error bars in Figures 2*b* and 2*c*.

We treat all gas and all dark matter in any cell which contains a galaxy subunit as belonging to that galaxy, so that association has an effective smoothing length of 0.5–1.0 h^{-1} Mpc. If the associated cool gas mass is less than $10^5\ M_\odot$, then $10^5\ M_\odot$ is assigned to it. Results, for the dependence on baryonic galaxy mass, are shown in Figures 3*a* and 3*b*. Total mass is well correlated with the stellar baryonic mass, but cool gas tends to be anticorrelated with a very large dispersion. In Figure 3*b* the dashed line shows the global average total-to-baryonic mass ratio, Ω_{tot}/Ω_b. We see that the most massive systems, $m_{tot} = 10^{12}$–$10^{13}\ M_\odot$, approach this average, but the dwarf systems with $m_{tot} = 10^8$–$10^9\ M_\odot$, have an order of magnitude more dark matter associated with them than expected on the basis of their baryonic stellar mass. The reason for this is presumably that they were made in regions where galaxy formation was inefficient (low-density regions; see Paper I, Fig. 4*a*, and Paper II, Fig. 9). As seen from the upper panel, much cool gas remains associated with the dwarf systems and systems with stellar mass $M \leq 10^{8.5}\ M_\odot$ contain more mass in cool gas than in stars. The reason for the decline in the amount of cool gas with increasing total mass is that the massive systems tend to collect in clusters filled with X-ray–emitting hot gas, so the associated cool gas is swept out or shock-heated during infall.

Resolution of the present code is not good enough to permit any meaningful statements to be made about the size, internal velocity dispersion (or rotation curve), or angular momentum of our galaxies.

Thus old systems tend to be massive and gas-poor, but dwarf systems tend to be gas-rich. Figure 3*b* shows that, although dark matter is correlated with luminous matter, the dwarf systems contain relatively more dark matter. Salucci, Ashman, & Persic (1991) find that the ratio of baryonic to dark matter in galaxies with well-measured rotation curves changes in the sense given by Figure 3*b*: "a strong monotonic increase of dark matter content with decreasing galaxy luminosity."

3.2. *Where Are Galaxies Formed? Bias and the Density Morphology Relation*

In Paper I we addressed the physical location of galaxies in two ways. In comparing the power spectra of the galaxies to the dark matter (Figs. 2*a* and 2*b* of that paper), we saw that

© American Astronomical Society • Provided by the NASA Astrophysics Data System

1993ApJ...417..415C

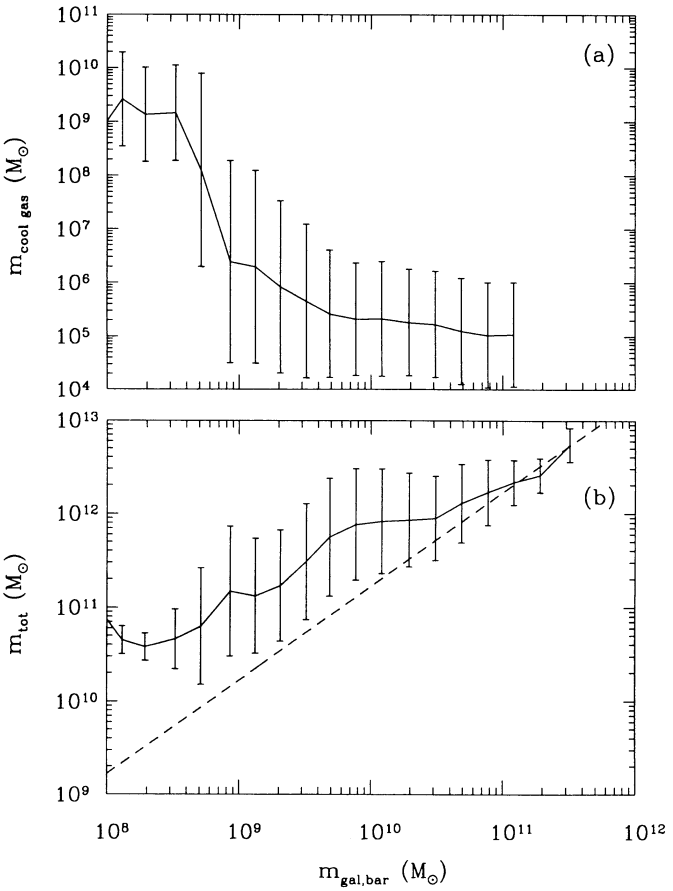

FIG. 3.—(*a*) Mass in cool gas associated with the galaxy vs. the galaxy mass in stars: low-mass galaxies have relatively and absolutely more cool gas. (*b*) Total mass associated with the galaxy vs. the galaxy mass in stars. While there is a rough proportionality between the two masses, the dwarf systems contain relatively more dark matter than do the giants.

clumping of the galaxies was greater than that in the total mass density with integral bias, $\sigma(\mathrm{gal})/\sigma(\mathrm{mass})$, ranging from 1.5 to 1.6 on 8 h^{-1} Mpc and larger scales to ≥ 1.7 on small scales. The ratio of the amplitudes of the power spectra (galaxies/dark matter) gives a differential measure of the same quantity. This reaches 6.7 on the 1 h^{-1} Mpc scale, where we become resolution-limited. Alternatively, we examined the ratio of (galaxy/total mass) as a function of both the galaxy and the mass densities, noting that the simple prescriptions for bias occasionally adopted do not seem appropriate. Neither a clipped nor a proportional model seemed correct. A simple fit to the ridgeline of the apparent relationship (see Fig. 4*a* of Paper I) can be made in the form

$$\log\left(\frac{\rho_g}{\langle\rho_g\rangle}\right) = A + B\log\left(\frac{\rho_{\rm tot}}{\langle\rho_{\rm tot}\rangle}\right) + C\left[\log\left(\frac{\rho_{\rm tot}}{\langle\rho_{\rm tot}\rangle}\right)\right]^2, \quad (2)$$

with (A, B, C) dependent, of course, on the Gaussian smoothing length ($R_{\rm sm}$) adopted. Table 1 shows these coefficients for a variety of Gaussian smoothing lengths and an estimate of the logarithmic dispersion σ about the mean line (base 10 log used throughout). Equation (2) provides an excellent fit to our numerical results for the range $0.3 \leq (\rho_{\rm tot}/\langle\rho_{\rm tot}\rangle) \leq 2000/R_{\rm sm}$, with typical error of the fit less than $\sigma/3$. For $\rho_{\rm tot}$ below the indicated range equation (2) underestimates galaxy density; for

TABLE 1

GALAXY BIAS VERSUS SMOOTHING RADIUS[a]

$R_{\rm sm,Gaussian}$ (h^{-1} Mpc)	A	B	C	σ
1	−0.90	2.00	−0.18	0.25
3	−0.40	1.70	−0.18	0.15
5	−0.20	1.50	−0.14	0.12
10	−0.10	1.44	−0.14	0.10
20	−0.05	1.40	−0.14	0.10

[a] Cf. eq. (2).

$\rho_{\rm tot}$ above the indicated range the last term on the right-hand side of equation (2) should be dropped.

Note that (ρ_g, $\rho_{\rm tot}$) represent the densities at redshift zero. The densities at the epochs when the galaxies were formed may have been quite different. The highest density regions are not necessarily the best places for making galaxies, but they correspond, because of Poisson's equation, to be deepest potential wells, and so galaxies collect in such regions. The fact that B is greater than 1 expresses the nonlinear nature of the physical bias which we have found. With small smoothing length we find that $\rho_{\rm gal} \propto \rho_{\rm tot}^2$, which is curiously reminiscent of the situation with regard to star formation in the Galaxy ("Schmidt's law;" Schmidt 1959 [also see Kennicutt 1990 for a modern discussion]) and may reflect the quadratic nature of radiative cooling. The dependence falls to $\rho_{\rm gal} \propto \rho_{\rm tot}^{1.4}$ when the smoothing scale reaches 20 h^{-1} Mpc. (For an alternative form of presentation of the results shown in Fig. 4*a* of Paper I look ahead at Fig. 14 of this paper).

Now we turn to a more pictorial discussion, focusing on one particular slice of size $80 \times 80 \times 10$ h^{-3} Mpc^3. Figure 4*a* shows a sample of $N = 6023$ randomly chosen dark matter particles projected onto one of the square faces of the volume, and Figure 5*a* shows the galaxy positions ($N = 6219$). While Figure 4*a* is similar in appearance to the results of other CDM simulations using the PM formalism (Efstathiou et al. 1985; Park 1990; Gelb 1992), Figure 5*a* is strikingly different. The clusters are more prominent, the voids are more empty, and they are demarcated by quite thin filaments which are "sharper" than any features seen in the dark matter slice. It is as if the latter were an out-of-focus version of the former. The actual sizes of the features are similar to those seen in, for example, the CfA maps of Geller & Huchra (1989). We will return to a more quantitative treatment later.

We have found it quite useful to break up the galaxies into four quartiles ordered according to $\langle t_i\rangle$, their birth date, labeled I, II, III, IV and displayed separately in Figure 5. Figure 5b displays the most recently formed quartile (I) of $N = 1550$ galaxies assembled later than $z = 2.0$. We see a *relatively* uniform distribution (while avoiding the voids) without prominent clustering. Figure 5*c* shows quartile II born in the interval $2.0 < z < 2.7$. The filament intersections are beginning to appear. In Figure 5*d*, quartile III, $2.7 < z < 3.6$, the clusters are stronger but the filaments are still evident, while in Figure 5*e*, the oldest quartile (IV), born in the interval $3.5 < z < 7.5$, all the galaxies are in the tightly bound clusters.

The differences in the spatial distribution of these populations, ordered by age, are quite impressive. Two possible explanations arise: (1) galaxies are always formed along the caustics, but they drift in time under the influence of gravity toward the vertices (i.e., clusters), where the gravitational potential is deepest; or (2) galaxies at high redshift are formed

© American Astronomical Society • Provided by the NASA Astrophysics Data System

1993ApJ...417..415C

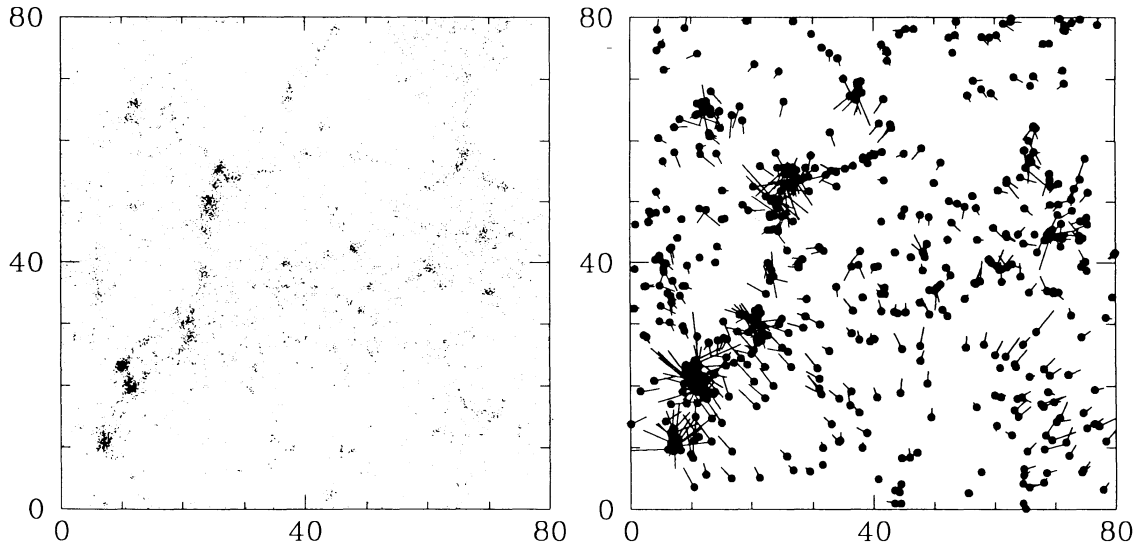

FIG. 4*a* FIG. 4*b*

FIG. 4.—(*a*) Positions of a set of randomly selected dark matter particles ($N = 6023$) in a slice with volume $80 \times 80 \times 10\ h^{-1}$ Mpc^3. (*b*) A random 10% of those dark matter particles with velocities indicated by arrows. Each dot indicates the position of a particle with the tail of the velocity vector attached to it.

at the vertices, where the density fluctuations first became nonlinear, but later can form along the caustics, which correspond to somewhat smaller values of $\delta\rho/\rho$. To test which, if either, of these explanations, is correct, we plot in Figure 5*f* the approximate positions of the progenitor galaxies (quartile IV) shown in Figure 5*e* at an earlier epoch, shortly after they were formed, $z = 3.6$. (An exact correspondence is not possible, because of mergers in the interval $z = 3.6$ to $z = 0.0$). Figure 5*f* is very unlike Figure 5*e* and much more like Figure 5*a*, quartile I, the distribution of younger galaxies shorter after their birth (i.e., now).

Thus, clearly, the preferred explanation is that galaxies form along caustics and drift into the clusters. This is plausible on a physical basis, because the hot gas in the vertices is the most unsuitable environment for galaxy formation even if the density is large (cf. Fig. 11 of Paper II). We have tried a similar

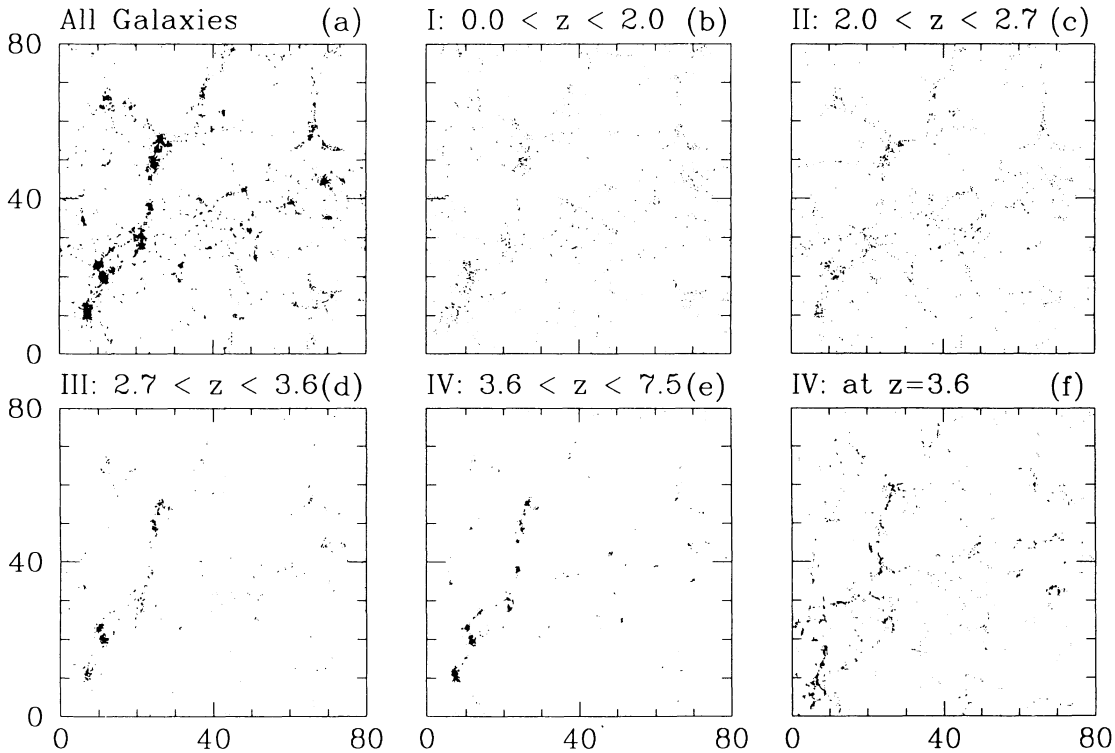

FIG. 5.—(*a*) Galaxy positions ($N = 6219$) projected onto one of the square faces of the volume. (*b*) The most recently formed quartile of N galaxies assembled more recently than $z = 2.0$. (*c*) The quartile born in the interval $2.0 < z < 2.7$. (*d*) The quartile born in $2.7 < z < 3.6$. (*e*) The oldest quartile, born in the interval $3.6 < z < 7.5$. Notice the increasing clumping with increasing age; we designate those in (*b*) and (*c*) "spirals," those in (*d*) "S0's," and those in (*e*) "ellipticals." In (*f*) are shown the positions of the progenitor galaxies (quartile IV) at $z = 3.6$.

© American Astronomical Society • Provided by the NASA Astrophysics Data System

1993ApJ...417..415C

exercise, where we divided the galaxies into four groups according to mass instead of age. A similar result was found, with the most massive objects tending to be found in the clusters and the lowest mass objects more uniformly distributed along the filaments. This result is not surprising, since, as we saw in Figure 2*b*, mass and age are correlated for the galaxies, so Figure 5 should translate into a similar one based on a division into mass categories. The fact that the differences seen among the different panels of Figure 5 are greater than those seen in the analogous figure based on mass quartiles makes us believe that age is the primary variable accounting for the spatial segregation.

Returning now to Figure 4, the dark matter slice, the right-hand panel (Fig. 4*b*) shows the projected velocity vectors of a random 10% of the particles shown in Figure 4*a*. Each dot indicates the tail of a velocity vector. Outside of clusters very large-scale coherent flows are seen. On the caustics where galaxy formation seems to occur, the velocity dispersion is very small.

It is tempting to interpret the properties of the galaxies in terms of observed morphology, given the correlations we have found among the variables of age, mass, and gas content. It is easy to show that elliptical galaxies are definitely on average more massive than spiral galaxies (cf. data in Kormendy & Djorgowski 1989) within the half-light radii of both types. They are also, on average older than spirals insofar as there is less recent star formation in ellipticals. And they have, of course, much less cool gas within them than do their spiral counterparts. We will succumb to this temptation and test the hypothesis that the oldest quartile of the galaxies in our simulation should be roughly identified with ellipticals, the next quartile with S0's, and the younger half with spirals. A finer division (e.g., 10%:15%:75%) could, of course, be made but is inappropriate given the nominal accuracy of our present simulations.

So defined, how will the properties of the three groups agree with those of real elliptical, S0, and spiral galaxies? The clustering tendency shown in Figure 5 is qualitatively reassuring, as are Figures 2*b* and 3*a*. To test the idea more quantitatively, we checked how the fraction of the three types depended on galaxy density.

The dramatic result is shown in Figure 6*a*, where a 1 h^{-1} Mpc Gaussian smoothing length is utilized to define density. The resemblance to the classic result of Dressler (1980) is striking. Figure 6*a* shows that in the "field" ($n_g/\langle n_g\rangle \leq 10$) the ratios are 61% spirals, 23% S0's, and 16% ellipticals, whereas at highest overdensities (reaching 200), i.e., in the great clusters, the ratios are 12% spirals, 18% S0's and 70% ellipticals. As a corollary test, we note that there is the expected relation between age of formation and environmental density as shown in Figure 6*b*. Note also that in both panels of Figure 6 the results shown are weighted by the galaxy number density, as is the case with observational data. For each galaxy we define the local smoothed density $n_{\rm gal}$ to be the total number of galaxies within a 1 h^{-1} Mpc radius sphere including itself) divided by the volume of the sphere. Given that definition, $n_{\rm gal} \geq 5\langle n_{\rm gal}\rangle$.

Last, we turn to the correlation functions, the classic, quantitative measures of clustering. We will show the data in several ways. In Figure 7*a* we look at all galaxies and the most massive group, and in Figure 7*b* we break them into the same "elliptical," "S0," and "spiral" fractions as previously. We see that the amplitude and slope of the correlation function depends significantly on galactic age, and to some extent on mass. All galaxies have a correlation length of 5.7 h^{-1} Mpc and

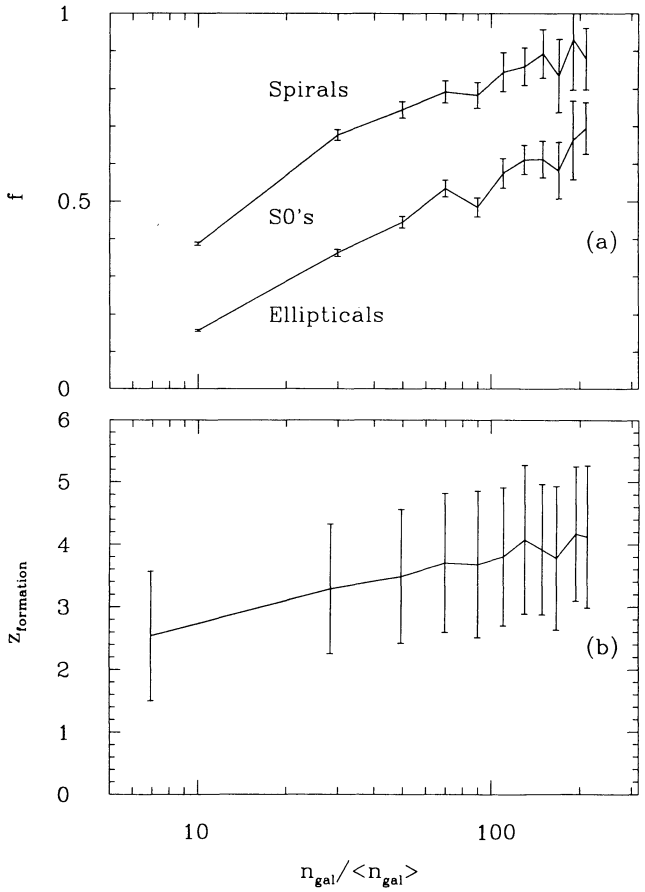

FIG. 6.—(*a*) Density-morphology relation, where a 1 h^{-1} Mpc Gaussian smoothing length is utilized to define density and we sample space by examining spheres surrounding galaxies. The resemblance to the classic result of Dressler (1980) is striking. It shows that in the "field" ($n_g/\langle n_g\rangle < 1$) the ratios are 61% spirals, 23% S0's, and 16% ellipticals, whereas at highest overdensity regions, i.e., in the great clusters, the ratios are 12% spirals, 18% S0's and 70% ellipticals. (*b*) Era of galaxy formation vs. its present local galactic number density, where the galaxy resides, with 1 σ error bars: old galaxies inhabit the dense regions.

are biased by about a factor of 2.5 compared with dark matter particles, but the youngest ones (not shown) are actually antibiased slightly. Both the slope and the amplitude of the spiral galaxy correlation function in Figure 7*b* match the data well. The correlation lengths of the two components are 4.5 h^{-1} Mpc for spirals and 8.5 h^{-1} Mpc for ellipticals + S0's, with a ratio of 1.9, and the ratio of the correlation length of ellipticals to that of all galaxies is 1.5. In an early study of this phenomenon in the real world Davis & Geller (1976) found that the correlation length for elliptical galaxies among themselves was 11.9 h^{-1} Mpc, for S0's it was 6.6 h^{-1} Mpc, and for spirals among themselves it was 4.4 h^{-1} Mpc, remarkably close to what we have found for our pseudomorphological types. We find a difference in slope between the ellipticals + S0's and spirals to be 0.35, with the older galaxies showing the steeper correlation function. Davis & Geller found the average for ellipticals and S0's to be steeper by 0.26 than that for the spirals.

3.3. *Velocity Information*

First we look at the simple distribution of proper velocities in differential and integral forms in Figures 8*a* and 8*b*. Also

© American Astronomical Society • Provided by the NASA Astrophysics Data System

1993ApJ...417..415C

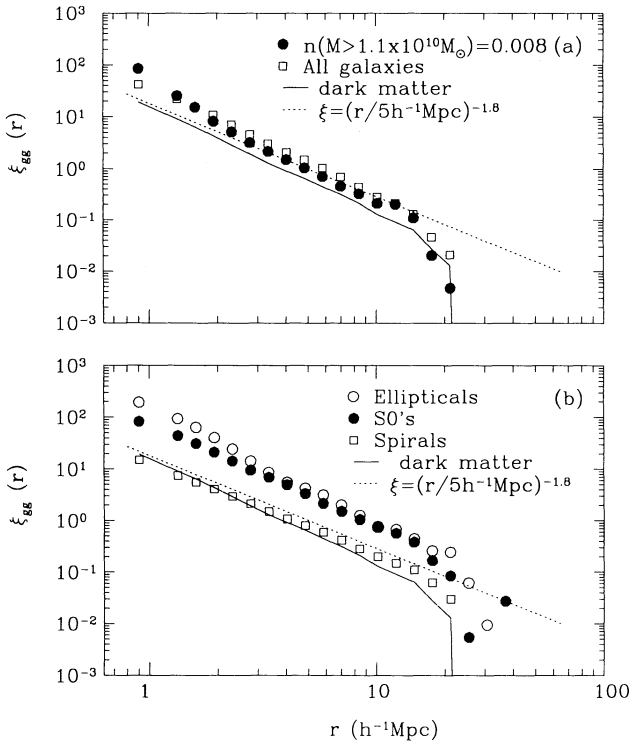

FIG. 7.—(*a*) Galaxy-galaxy two-point correlation functions for three sets of objects: most massive set of galaxies with density $n(M > 1.1 \times 10^{10}\ M_\odot) = 0.008\ h^{-3}$ Mpc^3, all galaxies, and dark matter particles. (*b*) Galaxy-galaxy two-point correlation functions for another four sets of objects: ellipticals, S0's, spirals, and dark matter particles. The dotted line indicates a power law with slope -1.8 and $r_0 = 5\ h^{-1}$ Mpc (Davis & Peebles 1983). Note that the older and more massive systems have steeper correlation functions than the younger and less massive systems, and the older ones also have a larger correlation length.

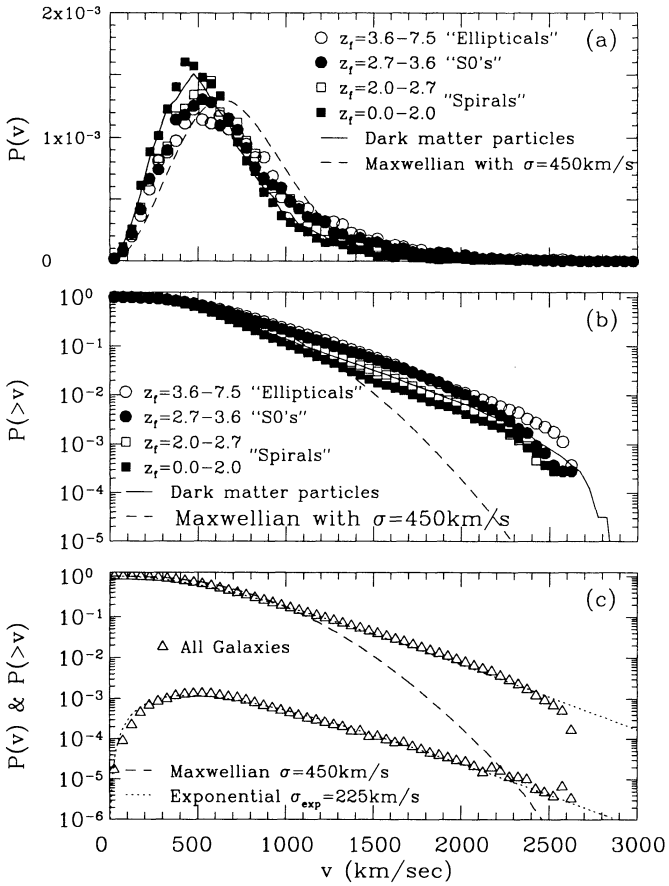

FIG. 8.—(*a*) Galaxy proper peculiar (three-dimensional) velocity distribution for four sets of galaxies ordered according to their formation epoch. Also shown is the distribution for dark matter particles (*solid curve*) and a Maxwellian fit for all the galaxies (*dashed curve*). (*b*) Integral counterpart of the distributions in (*a*). (*c*) Both differential and integral distributions for all the galaxies. Also shown are the exponential fits (both differential and integral forms) and Maxwellian fits (both differential and integral forms). The high-velocity tail of the distribution is much better fitted by an exponential (eq. [3]) than by a Maxwellian.

shown is the Maxwellian fit for all galaxies with three-dimensional dispersion $\sigma = 450$ km s^{-1}. We see that the older the galaxy, the greater the velocity dispersion, consistent with the environmental difference found earlier. The four quartiles had three-dimensional velocity dispersions of (490, 473, 439, 393) km s^{-1}, respectively. Figure 8*b* shows a surprising excess of large proper velocities (for all types) compared with a Maxwellian velocity distribution. This can, no doubt, be traced ultimately to the power-law–like nature of the initial spectrum of perturbations. An exponential fit is far better. Figure 8*c* shows the results for all galaxies compared with the distribution

$$f(v)dv = \frac{1}{8\pi\sigma_{\rm exp}^3}\, e^{-|v|/\sigma_{\rm exp}}\, dv\ , \qquad (3)$$

which gives $P(v) \propto v^2 e^{-v/\sigma_{\rm exp}}\ dv$. In Figure 8*c* the fits for all galaxies in both differential and integral forms are shown with $\sigma_{\rm exp} = 225$ km s^{-1}, and we see that the exponential fits are excellent. Separating them into age quartiles, we find $\sigma_{\rm exp} =$ (245, 237, 220, 197) km s^{-1} for the four types, respectively. Note that the velocity dispersion for each component is $(2)^{1/2}\sigma_{\rm exp}$. Davis & Peebles (1983, eq. [24]) have previously noted that observations are more consistent with an exponential than with a Maxwellian distribution. The net "velocity bias," which was described quantitatively in Paper I, is about 0.8, i.e., galaxies move slightly slower, on average, than do dark matter particles (see below).

Proper velocities are difficult to measure, since the true distance and hence the Hubble velocity are always insecure. Slightly easier is the pairwise velocity dispersion (since the Hubble velocity is common to adjacent objects). In Figure 9*a* we show the one-dimensional pairwise velocity dispersion (along the line connecting the pair) as a function of pair separation. We show separately the most massive galaxies, all galaxies, and dark matter particles. Also shown is the fit of the observational data from Davis & Peebles (1983). In Figure 9*b* we show the one-dimensional pairwise velocity dispersion for elliptical + S0 galaxies, spiral galaxies, and dark matter particles, respectively. Even though we use an amplitude significantly below that indicated by the *COBE* normalization and find a physical velocity bias, still the velocity dispersion of our simulated galaxies is significantly above those in observational samples. At 1 h^{-1} Mpc separation we find that the one-dimensional velocity dispersion of all galaxies is 670 km s^{-1}, with the brighter fraction somewhat lower at 490 km s^{-1}. These are significantly higher than the Davis & Peebles (1983) quoted value of 340 ± 40 km s^{-1}.

© American Astronomical Society • Provided by the NASA Astrophysics Data System

1993ApJ...417..415C

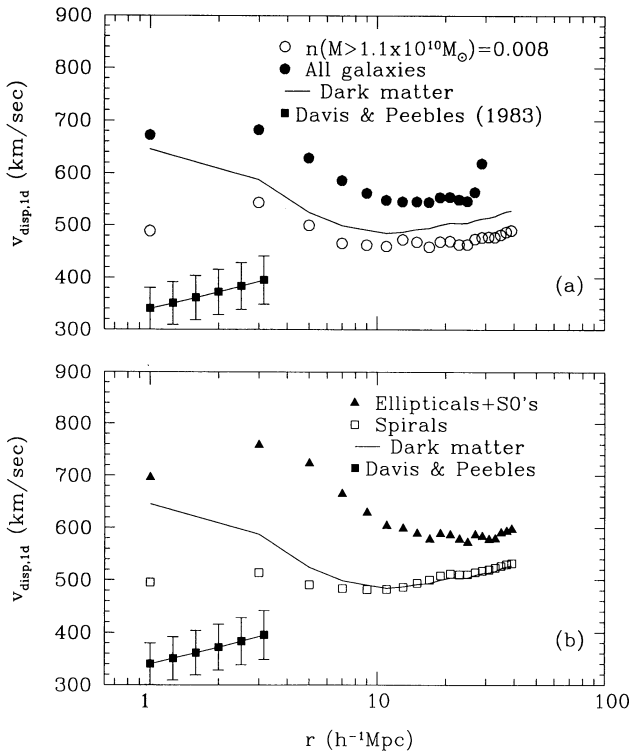

FIG. 9.—(*a*) Galaxy-galaxy one-dimensional pairwise velocity dispersion as a function of separation for three sets of objects: the most massive set of galaxies with density $n(M > 1.1 \times 10^{10}\ M_\odot) = 0.008\ h^{-3}$ Mpc^3, all galaxies, and dark matter particles. (*b*) Galaxy-galaxy one-dimensional pairwise velocity dispersion as a function of separation for two sets of objects: ellipticals + S0's, and spirals. The filled squares show the fit of the observed data (Davis & Peebles 1983), measured at $r < 1\ h^{-1}$ Mpc, and show a strong discrepancy at small $1\ h^{-1}$ Mpc scales.

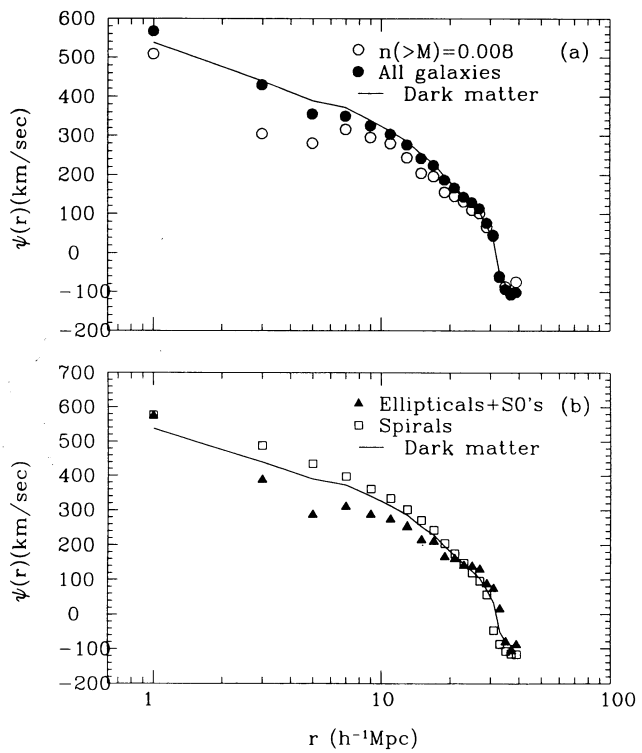

FIG. 10.—(*a*) Galaxy-galaxy scalar velocity correlation function as a function of separation of three sets of objects: the most massive set of galaxies with density $n(M > 1.1 \times 10^{10}\ M_\odot) = 0.008\ h^{-3}$ Mpc^3, all galaxies, and dark matter particles (*b*) Galaxy-galaxy scalar velocity correlation function as a function of separation for two sets of objects: ellipticals + S0's, and spirals.

Finally, in Figure 10 we look at the scalar velocity-velocity autocorrelation function defined as

$$\psi(r) = \text{sign}\,|\langle \boldsymbol{v}(\boldsymbol{x}) \cdot \boldsymbol{v}(\boldsymbol{x} + \boldsymbol{r})\rangle|^{1/2}\ . \tag{4}$$

The prefactor means that ψ is given the sign of the autocorrelation function. We group the data as in Figure 9. Observational data (Groth, Juszkiewicz, & Ostriker 1989; Gorski et al. 1989) show lower velocities but rather large scatter. Velocity bias is weak or absent in this statistic as seen from a comparison between galaxy and dark matter curves.

3.4. *Pie Diagrams*

Here we attempt to model as closely as we can the CfA redshift surveys (Geller & Huchra 1989). The CfA-like slices are constructed in the following way. We adopt a baryonic mass–to–blue-light ratio of 2.4 (appropriate for galaxies in our larger box and chosen to give the same density of galaxies as in the CfA survey) and take a limiting magnitude $m_{B(0)} = 15.5$, the same value as used in the CfA survey. We randomly select a point within the simulated box and set up a coordinate system for an observer sitting at that point. The slices shown in this section are typical ones drawn from the simulation.

Figure 11*a* shows a CfA-like magnitude-limited redshift survey slice in real space for all the galaxies. Figure 11*b* shows the CfA-like magnitude-limited redshift survey slice in redshift space for all the galaxies. Figure 11*c* shows the CfA-like slice for the half consisting of older galaxies (ellipticals + S0's) in redshift space. Figure 11*d* shows the CfA-like slice for the half consisting of younger galaxies (spirals) in redshift space. Note the too-strong "fingers-of-God" effect in comparing Figures 11*a* and 11*b* due to the fact that the clusters have too large a velocity dispersion as compared with the real Abell clusters. Comparing Figures 11*c* and 11*d*, we see that the older (ellipticals + S0's) sample is deeper, due to the typically higher mass (and luminosity) of this subset.

3.5. *Void Probability Function*

Figure 12*a* shows the fraction of space empty [to specified levels of $n(r)/\langle n(r)\rangle$] enough to contain spheres of specified sizes for our massive galaxies with $n = 0.01\ h^3$ Mpc^{-3} comparable to the CfA survey (Vogeley, Geller, & Huchra 1991) at the absolute magnitude limit of -20.0 and at 5 and 10 h^{-1} Mpc levels in Hubble space. Also shown for comparison purposes are the corresponding functions for the dark matter in redshift space with the same number of objects (to be statistically comparable). The dramatic difference in the void probability between heavy and thin curves (at fixed underdensity) quantifies the difference seen in the emptiness of voids in Figures 4*a* and 5*a* and thus the extreme normalization of the bias (cf. also Fig. 14). Let us focus on the $R = 5\ h^{-1}$ Mpc void probability. The mean number of objects in the sphere is $\bar{N} = 5.6$, so the expected number if distribution were random (Poisson), would be $P_0 = e^{\bar{N}} = 0.39\%$. In the dark matter simulation we find (Fig. 12*a*) $P_0 = 10.0\%$, with the difference

© American Astronomical Society • Provided by the NASA Astrophysics Data System

1993ApJ...417..415C

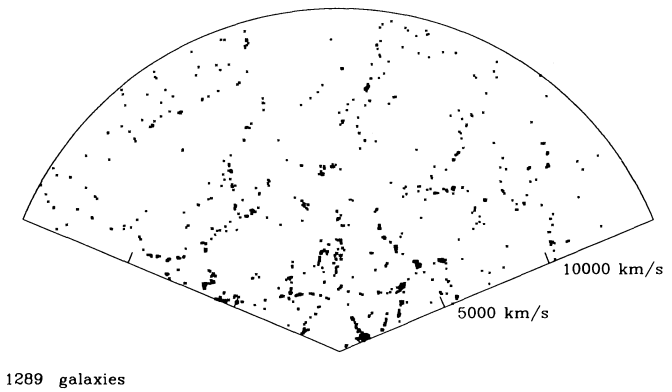

FIG. 11*a*

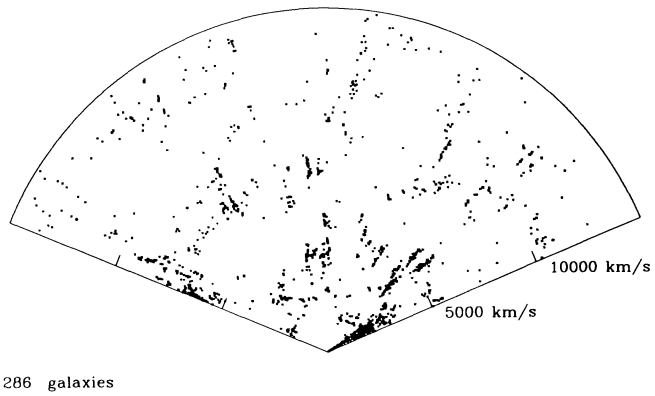

FIG. 11*b*

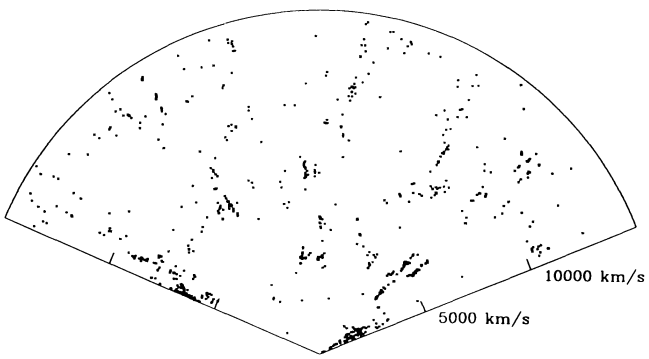

FIG. 11*c*

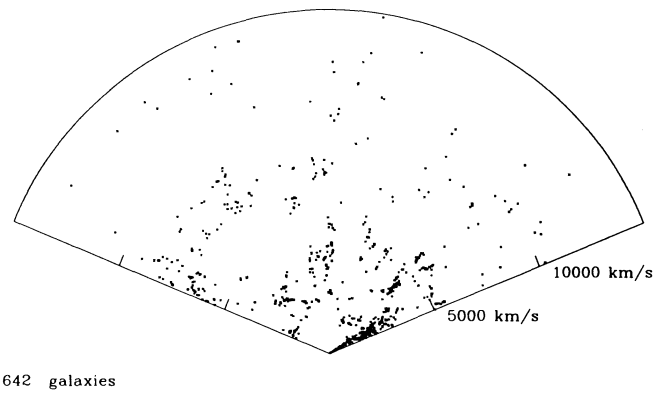

FIG. 11*d*

FIG. 11.—(*a*) CfA-like (Geller & Huchra 1989) magnitude-limited redshift survey slice in real space for all the galaxies. (*b*) CfA-like magnitude-limited redshift survey slice in redshift space for all the galaxies. (*c*) Same as (*b*), but for the half consisting of older galaxies (ellipticals + S0's). (*d*) Same as (*b*), but for the half consisting of younger galaxies (spirals). Note "finger of God" in (*b*).

($\times 25.6$) due to structure formation, e.g., correlations. But the galaxies show a void probability of $P_0 = 30.0\%$, an increase of another factor of 3.0. The emptiness of the voids is far greater than expected from the two-particle correlation function alone (formally all higher order correlation functions are needed to calculate the void probability), and it reflects the physical near-impossibility of making galaxies far from the caustics. Figure 12*b* shows the scaled void probability function as defined by Vogeley et al. (1991), and compared with their observations. Here we work in Hubble space and use a magnitude-limited subset of our galaxies similar to that shown in Figure 11*b*. The shaded area in Figure 12*b* represents the CfA observations (Vogeley et al. 1991, Fig. 7), the solid dots our simulation, and the dashed line the expectation for a Poisson distribution. We see that the simulation approaches the Poisson limits, as it should, on scales small compared with both the correlation length and the intergalaxy separation. Our result is consistent with observations. From $\bar{N} \sim 5$ to $\bar{N} \sim 40$ the scaled void probability function has a nearly constant slope; it corresponds roughly to a typical cluster size $N_{\rm cl} = 11.5$, shown as a heavy solid line ($P_0 = 0.35e^{-\bar{N}/N_{\rm cl}}$).

3.6. *Topological Distribution*

In a series of papers Gott and coworkers have developed a method to quantify topological distributions (Gott, Melott, & Dickinson 1986; Hamilton, Gott, & Weinberg 1986; Gott, & Mellot 1987; Weinberg, Gott, & Melott 1987; Melott, Weinberg, & Gott 1988). Their primary measure is the genus–threshold density relation. In applying their scheme to the distributions of galaxies and clusters in various redshift surveys (Gott et al. 1989), they found that the observed galaxy distributions are consistent with the initial random-phase density perturbation assumption.

We here apply their method to our simulated CDM galaxies. The data are smoothed with a Gaussian of $\sigma = 650$ km s^{-1} and the cell size is 125 km s^{-1} s^{-1}. Figure 13*a* shows the genus–threshold density relation for simulated, CfA-like magnitude-limited galaxies (for definition see § 4.3) in real space (*filled circles*) and in redshift space (*open squares*). Figure 13*b* shows the genus–threshold density relation for all the simulated galaxies in the box (volume-limited sample) in real space (*filled triangles*) and dark matter particles in real space (*open triangles*) with the same smoothing. The solid curves are fits of the theoretical expectation for a random-phase distribution. One sees that while the dark matter and all the galaxies have distributions consistent with random-phase initial conditions, the simulated, magnitude-limited galaxies, both in real space and in redshift space, show a small shift in the direction of the meatball topology, in agreement with analysis of the CfA redshift survey (cf. Fig. 7 in Gott et al. 1989).

We know that the initial conditions of our simulation were set up as a random-phase perturbation. So one is not surprised to see the result shown in Figure 13*b*. However, Figure 13*a* has much more interesting implications. It says that the

© American Astronomical Society • Provided by the NASA Astrophysics Data System

1993ApJ...417..415C

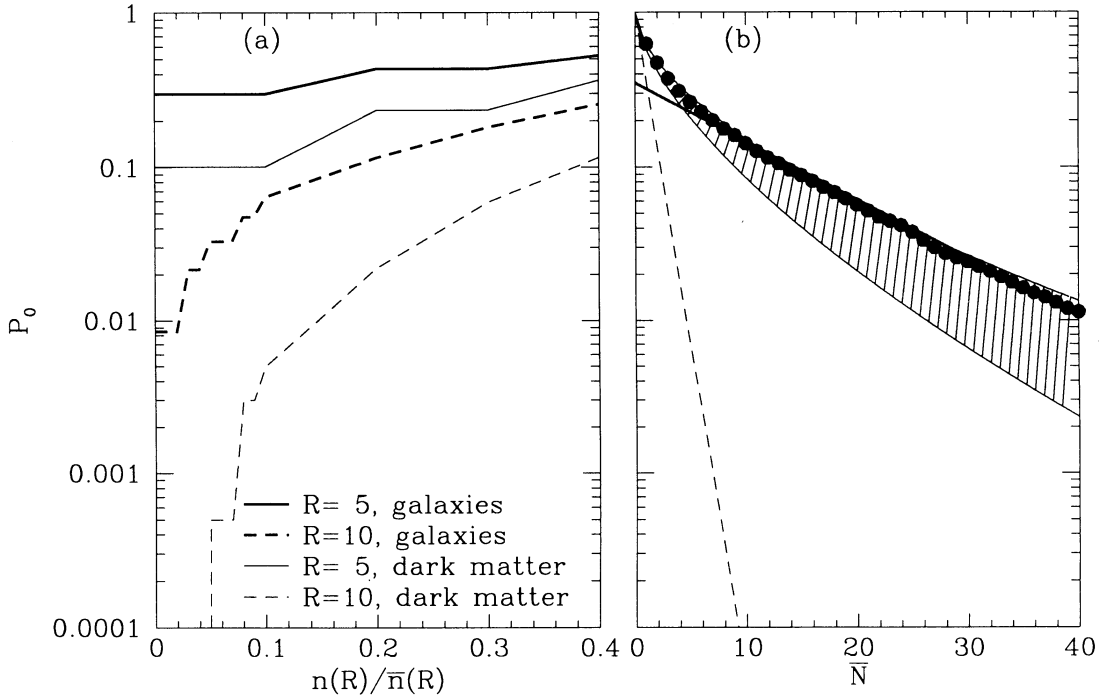

FIG. 12.—(*a*) Fraction of space empty [to specified levels of $n(r)/\langle n(r)\rangle$] enough to contain spheres of specified sizes for our massive galaxies with $n = 0.01\ h^3$ Mpc^{-3}) comparable to the CfA survey (Vogeley et al. 1991) at the absolute magnitude limit of −20.0 and at 5 and 10 h^{-1} Mpc levels. Also shown are the corresponding curves for randomly selected dark matter particles. (*b*) Scaled void probability function as defined by Vogeley et al. 1991. Here we work in Hubble space and use a magnitude-limited subset for our galaxies similar to that shown in Fig. 11*b*. The shaded area represents the CfA observations (Vogeley et al. 1991, Fig. 7), the filled circles our simulation, and the dashed line the expectation for a Poisson distribution. We see that the simulation approaches the Poisson limits, as it should, on scales small compared with both the correlation length and the intergalaxy separation. Our result is consistent with observations. From $\bar{N} \sim 5$ to $\bar{N} \sim 40$ the scaled void probability function has a nearly constant slope; it corresponds roughly to a typical cluster size of $N_{\mathrm{cl}} = 11.5$ shown as a heavy solid line ($P_0 = 0.35e^{-N/N_{\mathrm{cl}}}$).

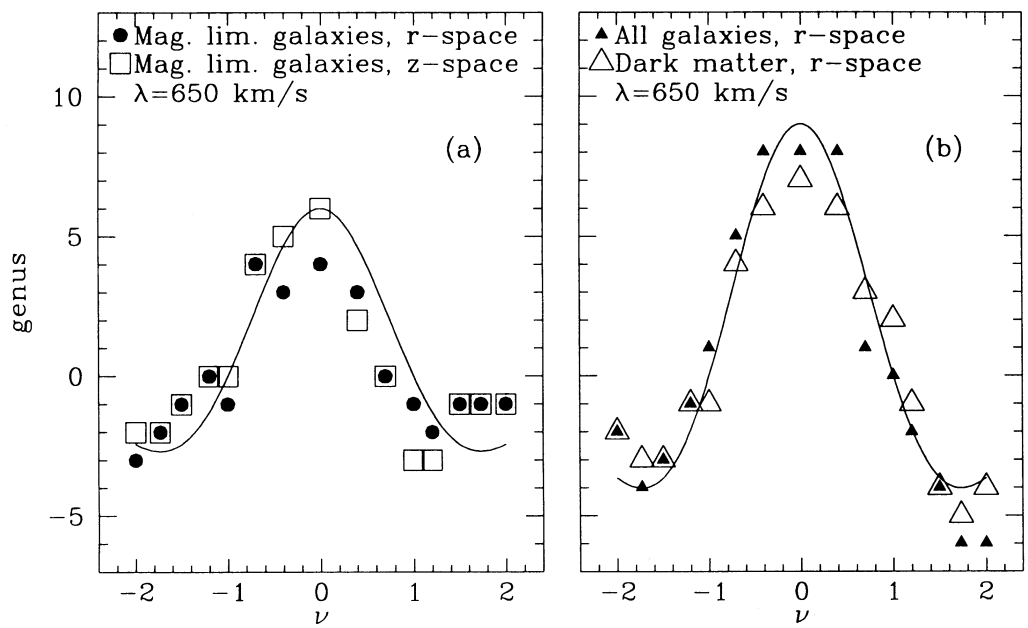

FIG. 13.—(*a*) Genus curve: genus as a function of threshold density value for our simulated magnitude-limited galaxies in redshift space (*open squares*) and in real space (*filled circles*) (*b*) Genus curve for all the galaxies in real space (*filled triangles*) and dark matter particles in real space (*open triangles*). The same number of dark matter particles as of galaxies are selected for comparison purpose in the simulated box. Note that the volume-limited samples are consistent with the expectation for a Gaussian random process (*solid lines*) but that the magnitude-limited sample shows the same "meatball shift" toward clumpiness as do the real data (Gott et al. 1989). The data is smoothed with a Gaussian of $\sigma = 650\ \mathrm{km\ s}^{-1}$, and the cell size is $125\ \mathrm{km\ s}^{-1}$.

© American Astronomical Society • Provided by the NASA Astrophysics Data System

1993ApJ...417..415C

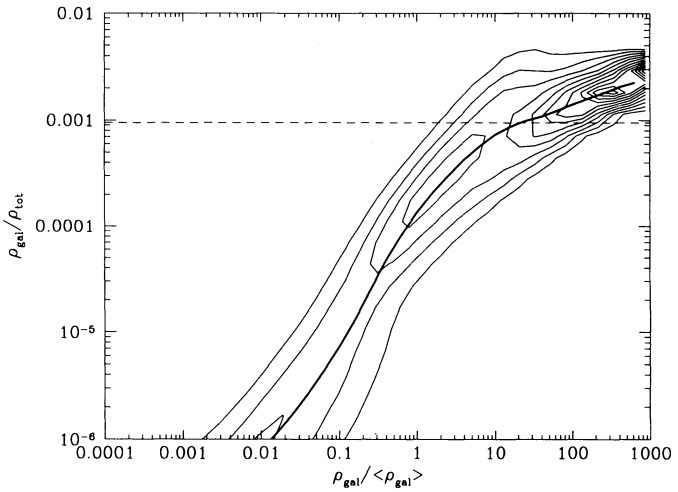

FIG. 14.—We show ρ_{gal}/ρ_{tot} as a function of the local galaxy density $\rho_{gal}/\langle\rho_{gal}\rangle$. The quantities are smoothed with a Gaussian of $\sigma = 1\ h^{-1}$ Mpc. The dashed line is the mean value. The strong trend shown is a direct portrayal of "bias."

magnitude-limited samples are biased to produce a meatball-like topology even though the underlying mass distribution or the initial mass perturbation has random-phase Gaussian nature. The reason for this shift is that the magnitude-limited samples have preferentially contained more massive, luminous (elliptical and S0) galaxies, which are more clustered (cf. Figs. 5 and 7) than all the galaxies as well as the spirals, i.e., further in the direction of meatball topology than all the galaxies or spirals.

3.7. *Velocity and Density Data Combined: Estimating* Ω

To the extent that we trust our simulations to compute correctly the relative galaxy formation efficiency and bias, we can use them, with observed data, to estimate Ω. The argument proceeds in a way similar to that used by White (1991) and the present authors in the previous paper, where X-ray–emitting gas was used as the tracer. Figure 14 shows that in the rich clusters the bias of galaxies in clusters $(n_{gal}/\langle n_{gal}\rangle)/(\rho_{tot}/\langle\rho_{tot}\rangle)$ is approximately 2–3. Observations indicate (Peebles 1986) that $\Omega \approx \langle M/L\rangle_{gal}/1200\ h$, and clusters are often used to estimate the mass-to-light ratio of galaxies. The "bias factor" quoted above, although not exactly what is required to translate cluster data to cosmic averages, should be useful in that effort.

4. CONCLUSIONS

When gas in cells is Jeans-unstable, cooling and collapsing, we allow it to condense, irreversibly, into galactic subunits, which we then follow with our collisionless PM code as they move under the influence of gravity (due to dark matter, gas, and other galaxy subunits). Grouping these subunits into galaxies with an adaptive friends-of-friends algorithm, we derive an acceptable mass function that fits (after combining the results of the small and large boxes) a Schechter function with $M_{bar}/L_B = 3$ (cf. Fig. 1*b*). Thus our galaxy formation algorithm combined with the CDM initial power spectrum produces reasonable results. The galaxies are typically assembled at $z = 3$–2, but a nontrivial fraction are made even earlier than $z = 6$.

Galaxy properties are strongly correlated with the epoch of formation, the (currently) most massive ones being formed earliest and the most gas-rich ones latest (Figs. 2*b* and 2*c*). Both of these properties are similar to what we infer from observations, and neither follows, in any obvious way, from the CDM input spectrum as such.

We also find (Fig. 3) that the ratio of dark matter to stellar matter increases by a factor of 10 as the baryonic mass decreases from $10^{11.5}$ to $10^{8.5}\ M_\odot$, and that, in many of the systems with smallest stellar mass, cool gas mass exceeds star mass, again similar to observations.

Dividing galaxies into categories by age and labeling the older half E + S0 and the younger half Sp + Ir, we find a strong morphology-density relation. In maps and slices the younger galaxies are found to be relatively smoothly distributed (while avoiding the voids), and the older, more massive galaxies accumulating in the deep potential wells at the vertices, where they constitute the observed "cluster of galaxies" phenomena. The ratios Sp:S0:E depend on the local density (Fig. 6) in a way which is strikingly similar to what was found in Dressler's (1980) discovery paper. The E + S0 types have a larger correlation length and a steeper slope than the Sp component, again as observed.

Turning to velocity information, we find that a Maxwellian is a poor fit, but an exponential $P(v) \propto v^2 e^{-v/\sigma_{exp}}$ is quite good. This has important observational consequences, since, on the basis of the assumption that the true velocity distribution is Maxwellian, higher proper velocities are often disregarded as spurious, either because of contamination by foreground/background objects or because of simple observational error. As an example, from Figure 8 we see that 1% of the galaxies have proper velocities in excess of 2000 km s^{-1} compared with 0.02% for the Maxwellian with the same variance!

At the $1\ h^{-1}$ Mpc separation scale the dispersion of relative velocities is relatively well observed to be 340 ± 40 km s^{-1} (Davis & Peebles 1983), but our models, even with too low a normalization (less than the *COBE* value by 2 σ), and even with the velocity bias that we find, is significantly too high: 670 km s^{-1} for all the galaxies and 490 km s^{-1} for the most massive subset. Renormalizing to the *COBE* measurement, the discrepancy is worse as the predicted velocity dispersion becomes approximately (920 ± 160) km s^{-1}. *This is the single strongest observational contradiction to the standard CDM scenario.*

In an investigation of the topological genus distribution we find an intriguing result. In a volume-limited sample our simulated galaxies show a symmetric distribution similar to that found in the dark matter and to the Gaussian random-phase expectation (Fig. 13*b*). But our simulated magnitude-limited sample shows the same "meatball shift" toward isolated lumps as do the real data. This is due to the fact that this sample selects for old massive systems that have drifted into the vertices. The void probability function computed from our pseudodata also agrees with the real data analyzed by Vogeley et al. (1991).

Thus it appears that the physical treatment of galaxy formation adopted in this work provides natural explanations for numerous observational facts such as the density-morphology relation or the genus curves, or the galaxy proper-velocity distribution. This agreement between observation and theory provides qualitative support for the CDM scenario, but quantitatively that picture fails. The basic origin of the failure, which reappears in many separate, different forms, is that the CDM potential fluctuations and induced velocity field are too large

© American Astronomical Society • Provided by the NASA Astrophysics Data System

1993ApJ...417..415C

on the 1 h^{-1} Mpc level by an unacceptable amount. We expect that other plausible scenarios, such as PBI or open CDM, when studied to the same level of physical detail as the classic CDM model investigated here, will do as well as or better than this model in matching observational tests.

We are happy to acknowledge support from grants NAGW-765, NAGW-2448, and AST90-06958 and AST91-08103. We thank David Weinberg for letting us use his program to compute the genus curves and the referee Andrew Hamilton for useful suggestions and help in correcting an error. It is a pleasure to acknowledge NCSA for allowing us to use their Convex-240 and Convex-3880 supercomputers. Discussions with Jim Gunn, Jim Peebles, and David Weinberg are gratefully acknowledged.

REFERENCES

Baron, E., & White, S. D. M. 1987, ApJ, 322, 585
Cen, R. Y. 1992, ApJS, 78, 341
Cen, R. Y., & Ostriker, J. P. 1992a, ApJ, 393, 22 (CO92)
———. 1992b, ApJ, 399, L113 (Paper I)
———. 1993, ApJ, 417, 404 (Paper II)
Davis, M., & Geller, M. J. 1976, ApJ, 208, 13
Davis, M., & Peebles, P. J. E. 1983, ApJ, 267, 465
Dressler, A. 1980, ApJ, 236, 351
Efstathiou, G., Bond, J. R., & White, S. D. M. 1992, MNRAS, 258, 1P
Efstathiou, G., Davis, M., Frenk, C. S., & White, S. D. M. 1985, ApJS, 57, 241
Gelb, J. M. 1992, Ph.D. thesis, MIT
Geller, M. J., & Huchra, J. P. 1989, Science, 246, 897
Gorski, K. M., Davis, M., Strauss, M. A., White, S. D. M., & Yahil, A. 1989, ApJ, 344, 1
Gott, J. R., Melott, A. L., & Dickinson, M. 1986, ApJ, 306, 341
Gott, J. R., Weinberg, D. H., & Melott, A. L. 1987, ApJ, 319, 1
Gott, J. R., et al. 1989, ApJ, 340, 625
Groth, E. J., Juszkiewicz, R., & Ostriker, J. P. 1989, ApJ, 346, 558
Hamilton, A. J. S., Gott, J. R., & Weinberg, D. H. 1986, ApJ, 309, 1
Jameson, A. 1989, Science, 245, 361
Kennicutt, R. C. 1990, in The Interstellar Medium in Galaxies, ed. H. A. Thronson & J. M. Shull (Dordrecht: Kluwer), 405
Kormendy, J., & Djorgowski, S. 1989, ARA&A, 27, 235
Melott, A. L., Weinberg, D. H., & Gott, J. R. 1988, ApJ, 328, 50
Park, C. 1990, Ph.D. thesis, Princeton Univ.
Peebles, P. J. E. 1986, Nature, 322, 27
Salucci, P., Ashman, K. M., & Persic, M. 1991, ApJ, 379, 89
Schmidt, M. 1959, ApJ, 129, 243
Suto, Y., Itoh, M., & Inagaki, S. 1990, ApJ, 350, 492
Vogeley, M. S., Geller, M. J., & Huchra, J. P. 1991, ApJ, 382, 44
Walker, T. P., Steigman, G., Schramm, D. N., Olive, K. A., & Kang, H. S. 1991, ApJ, 376, 51
Weinberg, D. H., Gott, J. R., & Melott, A. L. 1987, ApJ, 321, 2
White, S. D. M. 1991, in Clusters and Superclusters of Galaxies, ed. A. C. Fabian (Dordrecht: Kluwer), 17

© American Astronomical Society • Provided by the NASA Astrophysics Data System